

## High-frequency dynamics and test of the shoving model for the glass-forming ionic liquid Pyr14-TFSI

Kira L. Eliassen <sup>1</sup>, Henriette W. Hansen,<sup>1,2,4</sup> Filippa Lundin <sup>2</sup>, Daniel Rauber <sup>3</sup>, Rolf Hempelmann,<sup>3</sup> Tage Christensen,<sup>1</sup> Tina Hecksher,<sup>1</sup> Aleksandar Matic,<sup>2</sup> Bernhard Frick,<sup>4</sup> and Kristine Niss <sup>1,\*</sup>

<sup>1</sup>“Glass and Time”, IMFUFA, Department of Science and Environment, Roskilde University, P.O. Box 260, DK-4000 Roskilde, Denmark

<sup>2</sup>Department of Physics, Chalmers University of Technology, Göteborg, Sweden

<sup>3</sup>Department of Chemistry, Saarland University, 66123, Saarbrücken, Germany

<sup>4</sup>Institut Laue-Langevin, 71 Avenue des Martyrs, F-38042 Grenoble, France



(Received 9 March 2021; revised 17 May 2021; accepted 1 June 2021; published 25 June 2021)

In studies of glass-forming liquids, one of the important questions is to understand to which degree chemically different classes of liquids have the same type of dynamics. In this context, room-temperature ionic liquids are interesting because they exhibit both van der Waals and Coulomb interactions. In this work we study the  $\alpha$  relaxation and faster relaxation dynamics in the room-temperature ionic liquid 1-butyl-1-methylpyrrolidinium bis(trifluoromethanesulfonyl)imide (Pyr14-TFSI). The paper presents quasielastic neutron and shear mechanical spectroscopy data measured over seven decades in frequency ( $10^{-3}$ – $10^4$  Hz). The use of these two methods in combination reveal the  $\alpha$  relaxation and four separate, faster modes. Two of these faster modes, based on the partial deuterations, can be assigned to the methyl group and the methyl end of the butyl chain of the cation. The neutron data are also used to determine the mean-square displacement (MSD) on the nanosecond timescale. It is shown that the temperature dependence of the MSD can account for the super-Arrhenius behavior of the  $\alpha$  relaxation as predicted by the shoving model [Dyre, *Rev. Mod. Phys.* **78**, 953 (2006)], similarly to what is seen in simpler glass-forming liquids.

DOI: [10.1103/PhysRevMaterials.5.065606](https://doi.org/10.1103/PhysRevMaterials.5.065606)

### I. INTRODUCTION

Room-temperature ionic liquids (RTILs) are salts with melting points below  $100^\circ\text{C}$  [1], typically composed of a large organic cation and an inorganic anion. Ionic liquids have attracted attention over the last decades due to their potential applications, e.g., as candidates for highly stable electrolytes in the next generation of energy-storage systems [2,3]. RTILs are also interesting from a fundamental point of view because they constitute an interesting class of liquids: due to the competition of Coulomb interactions and van der Waals interactions they exhibit structural correlations on nanometer length scales with a clear signal in small-angle x-ray scattering (SAXS). Two peaks in addition to the nearest-neighbor correlation peak are found in the range of momentum transfers of  $Q = 0.1$ – $0.5 \text{ \AA}^{-1}$  for the nonpolar domains and  $Q = 0.6$ – $1 \text{ \AA}^{-1}$  for the charge ordering, which is not found in ordinary liquids [4–10]. Ionic liquids are therefore ideal systems to test how changes in chemical interactions and structure influence the dynamics of liquids. Like many other liquids, ionic liquids can be supercooled and brought into the glassy state. Viscosity and conductivity of the supercooled ionic liquids have a marked super-Arrhenius temperature dependence which puts ionic liquids in the category of so-called fragile liquids [11,12].

The main relaxation in liquids is the  $\alpha$  relaxation which, like the viscosity, has a super-Arrhenius temperature dependence.

In addition to this, it has been found that complex systems like mono-alcohols and recently also other hydrogen bonding systems have a mode slower than the  $\alpha$  relaxation believed to be associated with the dynamics of the hydrogen bonding network [13–16]. Inspired by this, several studies have investigated whether the nanoscale structures in ionic liquids give rise to similar slow modes, and in fact, a mode slower than the  $\alpha$  relaxation has been demonstrated in 1-octyl-3-methylimidazolium tetrafluoroborate [17]. However, little attention has been paid to dynamics faster than the  $\alpha$  relaxation. The fast (high-frequency) part of the relaxational dynamics is the focus of the current paper. Moreover, we look into the connection between fast vibrational dynamics and the temperature dependence of the  $\alpha$  relaxation, which has been investigated in many other classes of liquids [18] but rarely in ionic liquids.

Dielectric spectroscopy is the standard technique for studying the frequency and temperature dependence of the relaxational dynamics in organic glass-forming liquids, but the relaxation signal is masked by ionic conductivity in the case of ionic liquids. For ionic liquids the dielectric modulus, which reveals translational ionic motions as peaks in the imaginary part of the modulus [19], is often studied [12,20–23]. To get direct information on the  $\alpha$  relaxation of ionic liquids other techniques like light scattering, neutron scattering, or shear mechanical spectroscopy must be applied. In this work, the two latter techniques are employed with focus on dynamics in the supercooled liquid. We find from frequency-dependent shear modulus data and incoherent neutron scattering that the RTIL 1-butyl-

\*kniss@ruc.dk

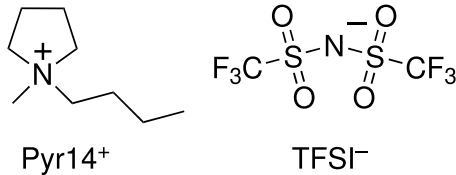


FIG. 1. A schematic of the sample Pyr14-TFSI with the cation to the left and the anion to the right.

1-methylpyrrolidinium bis(trifluoromethanesulfonyl)imide (Pyr14-TFSI) has as many as four different dynamic modes at higher frequencies than the  $\alpha$  relaxation. Yet the temperature dependence of the  $\alpha$  relaxation is connected to the vibrational mean-square displacement, as found in other classes of liquids and as predicted by the shoving model [18,24–26]. Moreover, earlier works have shown that Pyr14-TFSI obeys density scaling of both  $\alpha$  relaxation and viscosity and conductivity [27–29]. The overall picture is that while ionic liquids have additional structural features and rich dynamics, the  $\alpha$  relaxation which governs the transport properties and the glass transition has a behavior remarkably similar to that of other glass-forming liquids.

The paper is structured as follows. Section II presents the samples and the experimental techniques. The shear mechanical data and neutron inelastic fixed window scan data are presented in Secs. III and IV. The timescales of the modes found in the two techniques are compared to each other and to conductivity in Sec. V. In Sec. VI, the mean-square displacement is determined based on elastic fixed window scans, and these results are used in combination with the shear mechanical  $\alpha$ -relaxation times to test the shoving model in Sec. VII. The final section, Sec. VIII, contains a discussion of the results and conclusions.

## II. EXPERIMENTAL DETAILS

### A. The sample

The ionic liquid studied in this work is Pyr14-TFSI, which is well studied with various other techniques [6,27,28,30–37].  $T_m$  found from literature is 260 K [33], and  $T_g = 185$  K was measured in this work by differential scanning calorimetry (DSC), see Supplemental Material for details [38]. It has only a small degree of nanoscale structures due to the alkyl-chain lengths, which are visible in NMR measurements [31] but not in x-ray scattering experiments [6,10]; moreover the x-ray signal clearly shows a charge ordering peak [6]. It was found in this study that the supercooled sample is prone to cold crystallization at around 192 K in the shear measurements and 215 K in the DSC measurements.

The sample used in the shear mechanical study was of 99.9% purity, purchased from Solvionic and used as received. See Fig. 1 for an illustration of the sample. Previous studies [39] show that the liquid is highly hygroscopic and quickly absorbs water when exposed to atmospheric moisture; therefore all preparation and storage of the samples took place inside a glove box with inert nitrogen atmosphere.

For the neutron experiment the sample was synthesized with different degrees of deuteration in order to separate the dynamics of three parts of the cation: the pyrrolidinium ring,

the methyl group, and the butyl chain. The first, called D12, has both the butyl chain and the methyl group deuterated; D9 has the butyl chain deuterated, while D3 has merely the methyl group deuterated. The sample without deuteration was called D0 and is the same as the sample used in the shear measurements.

The deuterated samples were synthesized at the Department of Chemistry, Saarland University, Germany. The 1,1-dialkylated pyrrolidinium halide precursors used for the synthesis of the bis(trifluoromethanesulfonyl)imide ionic liquids were obtained by quaternization reactions of the corresponding 1-alkyl-pyrrolidines in acetonitrile under argon at ambient temperature for several days. 1-(d9-butyl)-pyrrolidine was synthesized by nucleophilic substitution of d9-butybromide with fivefold excess of pyrrolidine in acetonitrile at ambient temperature for five days, followed by purification via distillation. The methyl-deuterated precursor 1-butyl-1-(d3-methyl)-pyrrolidinium iodide was obtained by reaction of butylpyrrolidine with slight excess of d3-methyl iodide. 1-(d9-butyl)-1-methyl-pyrrolidinium bromide was obtained by reaction of slight excess of 1-methyl-pyrrolidine with d9-butybromide. 1-(d9-butyl)-1-(d3-methyl)-pyrrolidinium iodide was obtained by the reaction of 1-(d9-butyl)-pyrrolidine with slight excess of d3-methyl iodide. All halide salts were dried in high vacuum to remove the solvent and excess reagents, and their purity and identity was checked by multinuclear NMR spectroscopy. The halide precursors obtained this way were dissolved in water, and a slight excess of lithium bis(trifluoromethanesulfonyl)imide was added. After stirring for 18 hours the hydrophobic ionic liquids were extracted with dichloromethane, followed by washing the organic phase with water several times. The pure ionic liquids were obtained after removal of the solvent and drying in high vacuum for several days. Their purity was checked by multinuclear NMR spectroscopy, and the absence of residual halides was confirmed by testing with  $\text{AgNO}_3$  solution. See Supplemental Material for more detailed information about the synthesis of the three deuterated samples [38].

### B. Shear measurements

Frequency-dependent shear measurements were performed at Department of Science and Environment, Roskilde University, Denmark, using the piezoelectric shear modulus gauge (PSG) [40]. A version of the PSG with just one piezoelectric disk was used for these measurements. The PSG works by filling liquid in two gaps between two sapphire and a single piezoelectric (PZ) disk. An oscillating voltage is applied to the electrodes, causing the PZ disk to expand or contract radially due to the piezoelectric effect. The frequency-dependent capacitance of the PZ disk is measured and the shear modulus of the sample extracted therefrom [40]. The method works in the 1-mHz range up to as much as 40 kHz, and the capacitance of the disk was measured using the setup described in Ref. [41]; measurements were performed in a closed-cycle cryostat [42].

The sample is prone to cold crystallization and was therefore cooled rapidly down to 190 K, because previous tests showed no crystallization below this temperature. Subsequently, the spectra of the supercooled state were measured in cooling with 2-K steps from 190 to 180 K. Two frequency

TABLE I. The neutron cross sections for the four different samples D0 (fully protonated), D3 (methyl group deuterated), D9 (butyl group deuterated), and D12 (both methyl and butyl group deuterated). All scattering cross sections are in barn.

Sample	$\sigma_{\text{scat}}$	$\sigma_{\text{inc}}$	$\sigma_{\text{coh}}$	$\sigma_{\text{inc}}/\sigma_{\text{scat}}$ [%]
D0	1768	1606	161.3	91
D3	1545	1372	172.8	89
D9	1098	902.4	195.8	82
D12	875.1	667.8	207.3	76
TFSI	65.7	0.522	65.2	0.8

sweeps were made at each temperature, with a 10-min waiting time in between. Each spectrum takes 1 h if going to 10 mHz and roughly 10 h if going to 1 mHz. No change was observed between these two spectra, indicating that no crystallization is taking place. At 182 K,  $\log_{10}(\tau_{\alpha}/[s]) = 1.62$ . To avoid extrapolation we define this as the dynamic  $T_g$  for the shear measurements, since it is close to a relaxation time of 100 s.

Spectra in the glassy state (i.e., below 182 K) were measured on a new sample by cooling to 188 K, measuring a spectrum which collapsed with the previous 188-K data. Subsequently, the sample was cooled to 178 and 177 K for two additional spectra. The waiting time was 24 h before initiating measurements at 178 and 177 K. Two spectra were again measured at each temperature with each spectrum taking approximately 10 h, and no aging in the modulus was observed between the two spectra.

In addition to shear mechanical data, conductivity data were measured in the same cryostat as the shear measurements and with more data in the supercooled range than previously reported [30]. Details on the conductivity measurements can be found in the Supplemental Material [38].

### C. Neutron measurements

Quasielastic neutron scattering was performed on the backscattering instrument IN16B Institute Laue-Langevin (ILL), Grenoble. Elastic fixed window scans (EFWSs) were acquired with an energy resolution of  $\Delta E \approx 0.8 \mu\text{eV}$ , corresponding to a timescale of the dynamics of around 5 ns. Inelastic fixed window scans (IFWS) [43] were measured with an energy offset of  $E_{\text{IFWS}} = 2 \mu\text{eV}$ , giving a time of  $1/\omega_{\text{IFWS}} = 1/(E_{\text{IFWS}}/\hbar) = 3.3 \times 10^{-10}$  s. The  $Q$  range in both cases was  $0.19\text{--}1.90 \text{ \AA}^{-1}$ . The data were taken in cooling to avoid crystallization and covered the temperature range 10–310 K with a cooling rate of 0.5 K/min.

When using incoherent neutron scattering, it is often assumed in the analysis that no coherent scattering is present. This is a reasonable assumption for liquids containing a large fraction of hydrogen, since this element has a very high incoherent cross section. Deuterium, however, scatters only coherently, so an increased value of deuterium will decrease the incoherent cross section per molecular unit. Specifically, this will reduce the percentage of incoherent scattering from 91% in D0 to 76% in D12; see Table I for an overview of the incoherent contribution from each sample. The table also shows that the incoherent scattering from the TFSI anion can be neglected. Consequently, it is mainly the dynamics of the cation that is probed with inelastic neutron scattering in this

study. The type of dynamics expected from the cation will be a combination of (1) the global diffusion of the center of mass of the cation and (2) local motions due to ring wagging and segmental rotation of the butyl chain and the methyl arm [44].

The raw neutron-scattering data were reduced using the LAMP software package [45]. All EFWS and IFWS intensities were normalized to the elastic intensity at the lowest measured temperature.

### III. SHEAR MODULUS

Figure 2 shows the real and imaginary part of the shear modulus for Pyr14-TFSI in the temperature range 177–190 K plotted on a log-linear scale (a, b) as well as a log-log scale (c, d). Shear mechanical data on ionic liquids have been reported before, e.g., in [17,46], and for Pyr14-TFSI in particular by Palumbo *et al.* (2015) [47] and Tu *et al.* (2019) [23]. The main difference from these studies is that the frequency range in the isothermal spectra in this work is much larger, which makes it possible to also detect higher frequency relaxation modes in the ionic liquid.

The  $\alpha$  relaxation is seen as a rapid increase in the real part of the modulus and a prominent peak in the imaginary part. As expected, these features move to lower frequencies upon cooling.

The spectra, moreover, reveal a large  $\beta$  relaxation at high frequency near 10 kHz, a feature which is commonly seen in other liquids [48,49] but not earlier reported for ionic liquids due to lack of data in the relevant frequency range. The observed  $\beta$  relaxation is intense and appears to be temperature independent in position and amplitude in the liquid state, whereas it has a slight change in behavior in the glassy state. The low-frequency wing of the  $\beta$  relaxation is clearly resolved. However, different combinations of the high-frequency shear modulus,  $G_{\infty}$ , and the relaxation time of the  $\beta$  relaxation,  $\tau_{\beta}$ , gave fits of the same quality, which means that  $\tau_{\beta}$  and  $G_{\infty}$  cannot be well determined from these data.

In addition to the  $\beta$  relaxation, another feature located at around 0.1 Hz is also seen in the data. It has a low amplitude and only appears as a small shoulder around 182 K, becoming more evident in the glass at around 178 K. The mode appears to have weak or no temperature dependence but is merged with the  $\alpha$  relaxation, which makes it hard to judge.

In the time-temperature superposition (TTS) plot [inset of Fig. 2(c)], our data is compared to the data of Tu *et al.* [23]. There is good agreement between the spectral shapes of the two sets of data, but it is also clear that the two high-frequency modes,  $\tau_{\beta}$  and  $\tau_{\text{wing}}$ , are not resolved in data from Tu *et al.* and that our data are more precise/less noisy, especially at frequencies above the  $\alpha$ -relaxation peak.

At frequencies below the  $\alpha$  relaxation, the signal corresponds to viscous flow with the characteristic power-law behaviors in the real and imaginary parts [13]. This means that there is no slow mode, which is not surprising since x-ray scattering and simulation does not show a prepeak in this liquid [6,8].

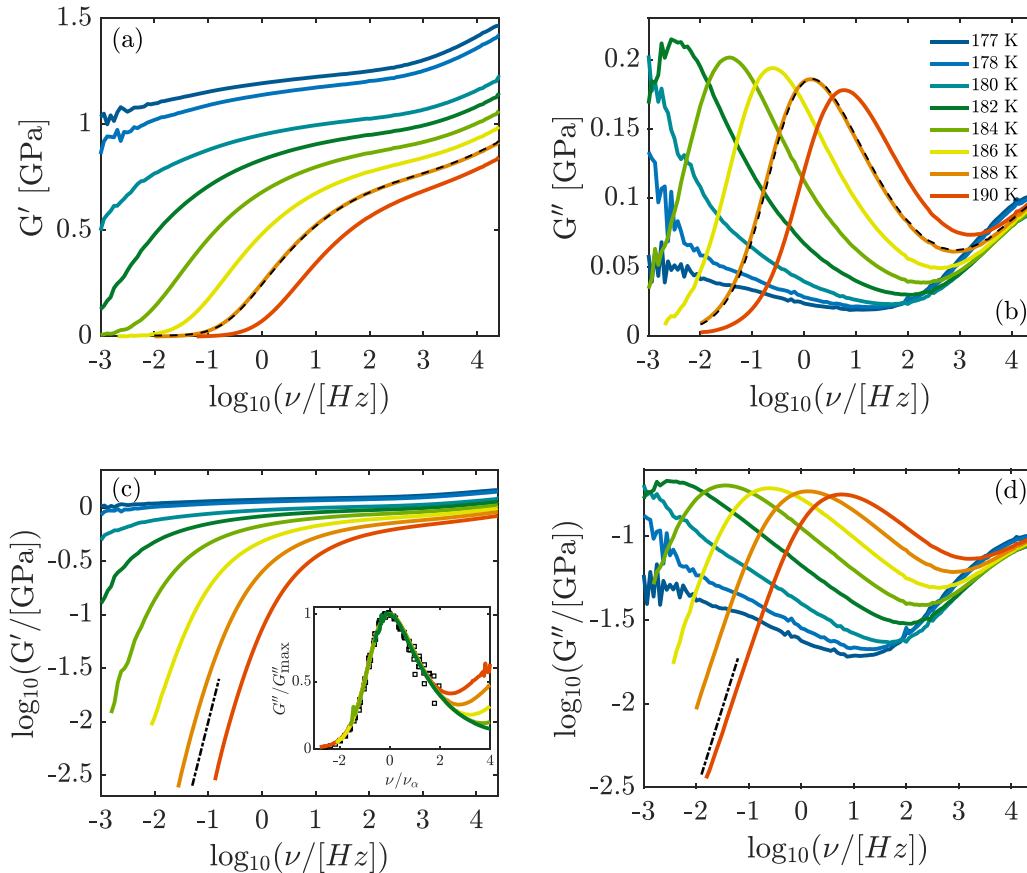


FIG. 2. The complex shear modulus of neat Pyr14-TFSI plotted as the (a) real part, (b) imaginary part, (c) logarithm of the real part, and (d) logarithm of the imaginary part. Data were taken at temperatures ranging from 177 to 190 K. The black dashed-dotted line illustrates the terminal, fully viscous behavior of a liquid at low frequencies. Black dashed line on top of the 188-K curve is from the second measurement at 188 K, which was followed by measuring in the glass at 178 and 177 K. Insert in (c) is a TTS plot of  $G''$  with data from literature (black squares) [23].

#### IV. QUASIELASTIC NEUTRON SCATTERING—FIXED WINDOW SCANS

Figure 3 shows temperature-dependent inelastic fixed window scans for the four different deuterations of the sample at different  $Q$  values. The incoherent scattering is in all cases well above 70%, and most of the signal can be assumed to come from hydrogen. This means that data on the D12 sample, which has both the butyl chain and the methyl group deuterated, mainly is sensitive to the pyrrolidinium ring dynamics, which we assume to couple to the center-of-mass motion of the cation and thus give direct information on the  $\alpha$  relaxation of the liquid. This main mode, around 300 K, is present in all four samples, whereas in D0, D3, and D9 the presence of other, additional modes, assumed to be connected to the butyl and methyl arm, appear at lower temperatures.

The high-temperature peak seen in all samples is clearly  $Q$  dependent, shifts to lower temperature, and decreases in intensity with increasing  $Q$  value, suggesting that the origin is diffusive [43]. This corroborates the interpretation that it is the  $\alpha$  relaxation of the liquid. The position of the low-temperature shoulders seen in the D9, D3, and D0 samples appears to be  $Q$  independent but increase in intensity with increasing  $Q$  values. This can be interpreted as the low-temperature mode being

due to local motions, consistent with the assumption that it originates from the butyl and methyl groups [43].

Thus our interpretation is that three different modes can be seen in the IFWS data of the nondeuterated sample. D0: The pyrrolidinium ring that is assumed to be coupled to the center of mass of the cation molecule, the methyl group motion, and the motion of the butyl group. This is also consistent with a recent interpretation of IFWS by Busch *et al.* [44]. In order to separate the different spectral contributions from each other, the data from the D12 sample have been fitted to a single Gaussian function at each  $Q$  value. The Gaussian is purely phenomenological but fits the data very well and can therefore be used to interpolate between data points. An example of the result can be seen in Fig. 4(a). The interpolation of the D12 data makes it possible to subtract the D12 intensity from the D3 and D9 intensity. Figure 4(b) shows the D3 and D9 data obtained through the following procedure: Fit the D12 data at each  $Q$  with a Gaussian function to establish the interpolation, subtract this from the D3 and D9 data at each  $Q$ , and then finally sum over all  $Q$  (see Supplemental for the result at individual  $Q$ ). This procedure makes it evident that the samples D3 and D9 indeed have dynamics separated from the main mode of the pyrrolidinium ring, visible as a peak in intensity at around 184 and 208 K, respectively.

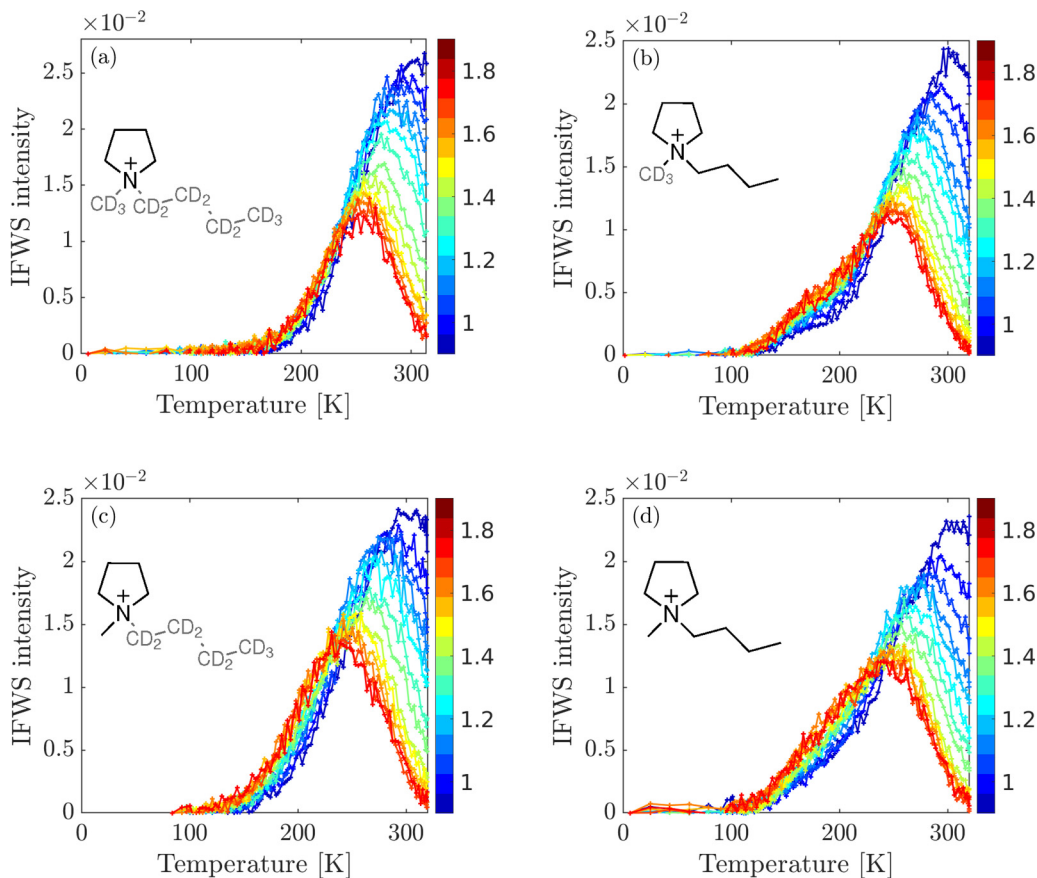


FIG. 3. IFWS intensity for the whole  $Q$  range (red to blue, see the color bar in units of  $\text{\AA}^{-1}$ ) and for all four Pyr14-TFSI samples: (a) D12, (b) D3, (c) D9, and (d) D0. Intensity was normalized (after subtracting background) to the lowest temperature elastic signal, and the four lowest  $Q$  values were excluded since the data here are very noisy and disrupted the whole picture of the  $Q$  dependence. The main peak present in all samples is  $Q$  dependent and decreases in intensity with higher  $Q$  values. Two additional,  $Q$ -independent modes appear to be present in the D3 and D9 sample, respectively, as shoulders at lower temperatures.

The simplest assumption is that these localized motions have a Lorentzian spectral shape which leads to the following

functional form of the IFWS signal [43,44]:

$$I(T) = e^{-aT} \left[ I_0 \frac{1}{\pi} \frac{\tau(T)}{1 + \tau(T)^2 \omega_{\text{IFWS}}^2} \right], \quad (1)$$

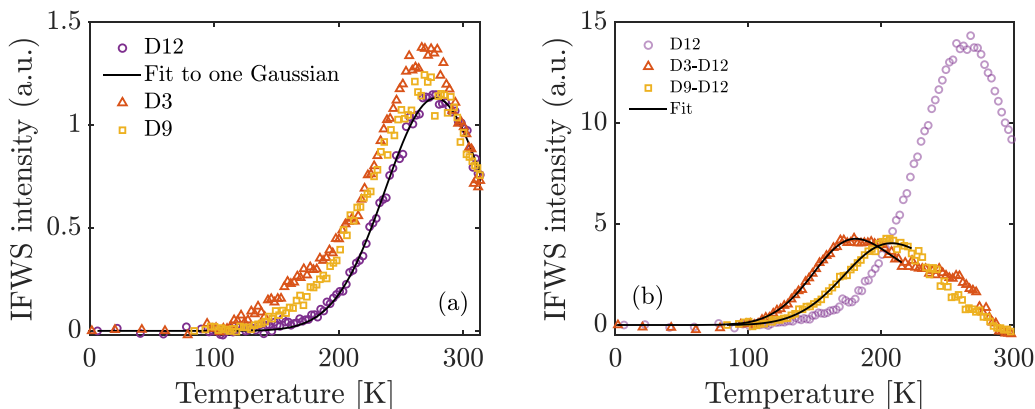


FIG. 4. IFWS intensity of Pyr14-TFSI as a function of temperature. (a) Data from the D3, D9, and D12 samples at  $Q = 1.3 \text{ \AA}^{-1}$  as an example. The data from the D12 sample (purple) is shown together with a fit to a Gaussian function (black solid line), showing excellent agreement between the two, meaning that the fit can be used as interpolation of the data. (b) IFWS intensity summed over  $Q$  for D12 and for D3 and D9, where the interpolation from the D12 sample has been subtracted at each  $Q$  in order to show additional dynamics that are separated from the main mode. Black solid lines are fit to the proposed model shown in Eq. (1).

where  $\tau(T)$  is the temperature-dependent relaxation time, and  $\omega_{\text{IFWS}}$  is the angular frequency given by the energy offset at which the data is acquired,  $\omega_{\text{IFWS}} = \Delta E/\hbar$ . The exponential prefactor is the temperature-dependent Debye-Waller factor and  $a$  is found from a fit to the low-temperature region of the EFWS intensity (see Supplemental Material [38]).

Assuming that the temperature dependence is Arrhenius in nature gives

$$\tau(T) = \tau_0 e^{E_a/RT}, \quad (2)$$

where  $R$  is the universal gas constant,  $\tau_0$  is the high-temperature limit of the relaxation time, and  $E_a$  the activation energy of the local dynamics. Combining Eqs. (1) and (2) gives a model with  $\tau_0$ ,  $E_a$ , and  $I_0$  as free parameters (in addition to  $a$ , which is found from the EFWS data). This approach for fitting IFWS data was proposed by Frick *et al.* [43] and has recently been used by Busch *et al.* to analyze IFWS data on a RTIL [44].

Figure 4(b) shows the fit (black solid lines) to the D3-D12 and D9-D12 data. The fit is only performed in a temperature range where the residual is at least 50% of the total signal, i.e.,  $(D3-D12)/D12 > 50\%$ . The model gives a convincing fit, and with a  $\tau_0$  in the picosecond range which is physically reasonable. The activation energies for the localized motions are found to be  $E_a = 7.8$  kJ/mol for the D3 sample and  $E_a = 9.1$  kJ/mol for the D9 sample. These activation energies show good correspondence with previous studies [44,50,51] on the fully protonated RTIL N-butylpyridinium bis(trifluoromethanesulfonyl)imide, which is a sample very similar to the one in this study, except that the cation ring only has the alkyl chain and not the methyl group.

It is worth noting that the local mode in D3 where the butyl is the visible alkyl group is faster than the mode of D9 where the methyl is visible. In addition, the two modes have similar intensity, even though the butyl has three times as many hydrogen atoms than the methyl. This leads to the conclusion that it is probably mainly the end methyl group that is active in the butyl mode seen here. This is in line with results and discussions in Ref. [50], where the part of the alkyl chain close to the aromatic ring in a similar cation can appear to be almost immobile on the timescale of the experiment. In Ref. [29] where the focus is on the pressure dependence and on the geometry of the dynamics of Pyr14-TFSI, it is found that there is also active dynamics in the picosecond timescale at room temperature. This is assigned to the conformational dynamics of the butyl chain and libration of the pyrrolidinium ring.

## V. TIMESCALES

To get an overview of the different dynamic modes which were seen in the shear mechanical and neutron scattering data, we collect them in a relaxation map/Angell plot in Fig. 5, where the relaxation time of the modes is shown as a function of normalized inverse temperature  $T_g/T$ , with  $T_g = 182$  K found from shear measurements.

The measurement of shear mechanical spectra over 7 decades in frequency per temperature makes it possible to track the  $\alpha$ -relaxation time,  $\tau_\alpha$ , with decreasing temperatures all the way down to the glass transition. The  $\alpha$ -relaxation

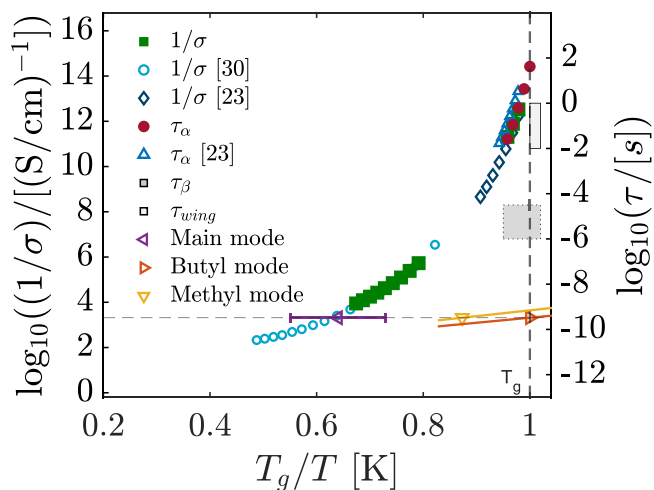


FIG. 5. Relaxation map showing the timescale and temperature dependence of the five different dynamic modes found in this study of Pyr14-TFSI. The inverse conductivity is a combination of data from literature (blue, open circles and diamonds) [23,30] and from this study (green, filled squares), plotted here together with the structural relaxation time from this study (red, filled circle) and from literature (blue, open triangles) [23]. Conductivity data from Martinelli *et al.* [30] have been scaled in absolute value in order to collapse with data from this study. Temperature is normalized to  $T_g$  as found from shear measurements (182 K). Note that the two different y axes have been shifted so that the shear modulus and conductivity measurements collapse in the supercooled regime and cover the same range (16 decades). The purple, orange, and yellow triangles show the three dynamic modes found from the IFWS intensity and are related to dynamics connected to the pyrrolidinium ring, the butyl group, and the methyl group, respectively (see details in Sec. IV). The error bar of the main mode represents the  $Q$  dependence of this. Solid lines are the Arrhenius dependence found from the model fits to the D3 and D9 data with the D12 interpolation subtracted. Dynamics of the pyrrolidinium ring, and thus the center-of-mass motion of the cation, is seen to be related to the  $\alpha$  relaxation (blue, green, and red). The dark gray square box is the  $\beta$  relaxation,  $\tau_\beta$ , and light gray box is the third relaxation,  $\tau_{\text{wing}}$ , found as a wing at low temperatures, both from the shear modulus.

time was found from the shear modulus data by a fit to a second-order polynomial around the  $\alpha$ -relaxation peak,  $f_{\text{max}}$ , and  $\tau_\alpha = 1/(2\pi f_{\text{max}})$ .

This gives information to calculate the isobaric Angell fragility index,  $m_p$ , from shear modulus measurements. The fragility index is given by [52,53].

$$m_p = \left. \frac{d \log_{10} \tau_\alpha}{d T_g/T} \right|_{T=T_g}. \quad (3)$$

For Pyr14-TFSI we find that  $m_p = 85$ , which is consistent with fragility found for other RTILs [12]. This value is also reasonably close to what Tu *et al.* found in their study of Pyr14-TFSI [23],  $m_p = 82$  with  $T_g$  defined as  $\log_{10}(\tau_\alpha/[s]) = 1$ .

In addition to the timescale axis, the relaxation map in Fig. 5 also includes an axis of the resistivity/inverse ionic conductivity. Conductivity data from this work are shown both in the supercooled region and in the liquid above the

melting point. Additional liquid data from literature are also shown. The pronounced cold-crystallization tendency leads to a “no-man’s land” just below the melting point where the liquid properties cannot be accessed.

The position of the inverse conductivity axis relative to the timescale axis is chosen such that the  $\alpha$ -relaxation time and inverse conductivity, from this study, collapse at 188 K. Subsequently, the two data sets at the other temperatures in the supercooled range follow each other closely, showing that the conductivity and the  $\alpha$ -relaxation time have the same temperature dependence. This behavior is qualitatively consistent when including conductivity and  $\alpha$ -relaxation data from literature [23]. A similar behavior is found by Jafta *et al.* [54] by comparing conductivity and  $\alpha$  relaxation measured by dielectric spectroscopy on 3-methyl-1-methylimidazolium bis(trifluoromethanesulfonyl)imide (DMIM-TFSI) with 1 mol Li-TFSI. This implies that ion translation and structural relaxation are directly coupled or governed by the same parameters. This is consistent with a study by Martinelli *et al.* showing coupling between  $T_g$  and conductivity in an ionic liquid [30]. At higher temperatures above the “no-man’s land,” the conductivity data from this study and from literature [30] have the same temperature dependence. Another way to represent the data is by comparing inverse conductivity and viscosity; see Supplemental Material [38] for a discussion of this.

The shear mechanical data do not allow for an exact determination of the timescales of the  $\beta$  relaxation nor of the additional mode seen between the  $\alpha$  and  $\beta$  relaxation in the shear data of the glassy sample. However, it is possible to estimate their position, and these are indicated with two gray areas in the plot and are denoted  $\tau_{\text{wing}}$  (light gray) and  $\tau_{\beta}$  (dark gray) for the middle and fast relaxation, respectively.

The neutron-scattering fixed window scan is a “single timescale” technique giving information on nanosecond dynamics, which is illustrated in the relaxation map as a dashed, horizontal line at  $\tau_{\alpha} = 1/\omega_{\text{IFWS}} = 3.3 \times 10^{-10}$  s. Three dynamic modes were identified with the IFWS method, and the temperature dependence of the main mode, which is directly related to the translational motion of the center of mass of the cation, was found by fitting the D12 data with a Gaussian function at  $Q$  values of 0.44–1.9  $\text{\AA}^{-1}$  and then assuming the peak position of the fit to be equal to the temperature of the main mode. This is seen as the purple triangle (average), with the error bars extending from the highest to the lowest temperature of the main mode, since the temperature dependence of the neutron signal is  $Q$ -dependent for the  $\alpha$  relaxation. This main mode of the cation fits very well with the shear mechanical  $\alpha$  relaxation and the resistivity. The orange and yellow lines, representing the dynamic mode from the butyl and methyl group, respectively, are calculated from the best-fit parameters found Sec. IV, assuming Arrhenius behavior. Both of these secondary modes are faster than the main mode and are assumed to have a  $Q$ -independent temperature dependence. The lines are seen to cross the  $1/\omega_{\text{IFWS}}$  line at triangles with the same color. These triangles are found from the  $T_{\text{max}}$  formula derived from the model in Eq. (1), see Frick *et al.* [43] for details.

In case of the neutron data the tool of partial deuteration has made it possible to assign the modes at low temperatures to movements in a particular part of the cation. In case of

the shear data there is no direct information on what part of the molecule(s) the modes are related to. However, based on the relaxation map (Fig. 5), it does not seem likely that the  $\beta$  relaxation nor the wing are connected to butyl or methyl dynamics, since the temperature dependence of the butyl and methyl modes is very low, and thus these modes are well separated from the  $\beta$  relaxation and the wing of the shear mechanical data. Even if the actual temperature dependence does not follow a simple Arrhenius behavior, it would require a stronger temperature dependence than that of the  $\alpha$  relaxation for the butyl and methyl mode to be connected to the  $\beta$  relaxation and the wing. This is inconsistent with the fact that the  $\alpha$  relaxation of a liquid is normally found to be the mode with the strongest temperature dependence. Moreover, the wing and the  $\beta$  relaxation in the Pyr14-TFSI spectra also appear to have very weak temperature dependencies in the range where they are detected. Therefore we conclude based on the relaxation map that four different relaxational modes are active at shorter timescales or equivalently, at lower temperatures than the  $\alpha$  relaxation. The origin of the  $\beta$  relaxation and the wing are open to speculation, but it could be related to anion dynamics or be so-called genuine Johari-Goldstein  $\beta$  relaxation [49,55]. A similar relaxation map is also seen in the study by Jafta *et al.* [54], where four distinct relaxation modes were detected by a combination of dielectric spectroscopy and neutron-scattering data.

## VI. MEAN-SQUARE DISPLACEMENT

So far the focus of the paper has been on relaxational dynamics. However, the elastic fixed window scans (EFWS) of the neutron data also contain information on the vibrational dynamics taking place at faster timescales than the nanosecond. In the following the EFWS data will be analyzed in terms of the mean-square displacement (MSD), and the extracted results will be connected to the temperature dependence of the  $\alpha$  relaxation in terms of the shoving model in Sec. VII.

### A. Finding the mean-square displacement from neutron data

A number of different approaches may be employed to determine MSD from the elastic incoherent scattering data. Common for all of them is that one fits the  $Q^2$  dependence of the logarithm of the normalized elastic intensity to a function that contains the MSD as a free parameter. The traditional way is to use the Gaussian approximation of scattering from liquids [56], where a linear relation between the logarithm of the normalized intensity and  $Q^2$  is assumed. Another method is one suggested by Zorn [57,58], which takes into account multiple scattering and the non-Gaussian character of the dynamics and has one less free parameter than the Gaussian approximation.

Figure 6 shows the normalized intensity as a function of  $Q^2$  at two different temperatures and deuteration. Fits to the Gaussian approximation are shown for two different  $Q$  ranges and it is seen that the Gaussian approximation breaks down as temperature is increased. In contrast to this, the data points at higher temperatures are well captured by the fit to the Zorn method. Furthermore, this method also seems more robust to the fact that a coherent signal enters as a shoulder at around

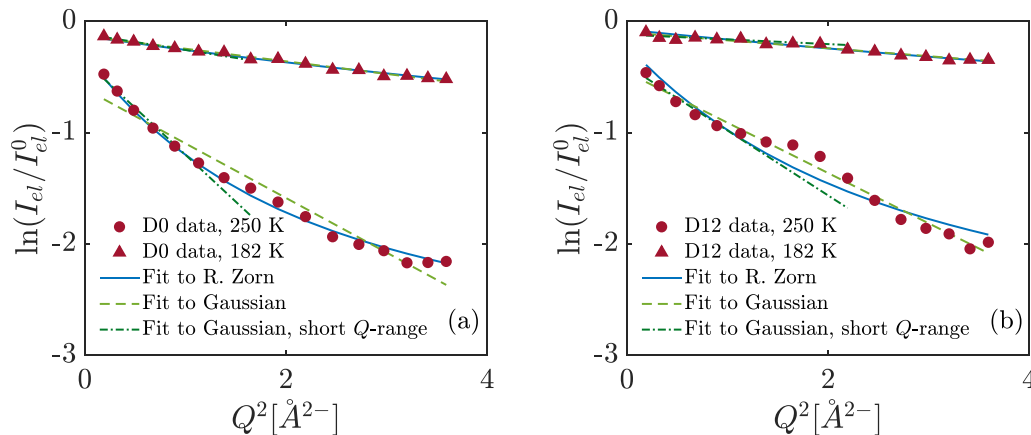


FIG. 6. Logarithm of the normalized intensity as a function of  $Q^2$  for Pyr14-TFSI with deuteration (a) D0 and (b) D12 at both 250 K (circles) and 182 K (triangles) in order to show the qualitative difference between the fits to data with the Gaussian method (green) and the Zorn method (blue). This plot also illustrates how a coherent signal slowly starts to increase at around  $1.9 \text{ \AA}^{-2}$  with increased deuteration.

$Q^2 \approx 1.9 \text{ \AA}^{-2}$  and grows with increasing deuteration (see next section). This coherent signal is also a reason for the resulting MSD being somewhat dependent on the chosen  $Q$  range in the Gaussian approximation, an effect that is most pronounced at higher temperatures. This leads to the conclusion that the Zorn method will be used to calculate MSD from the elastic incoherent scattering data in this study. See Supplemental Material for details [38].

### B. MSD data from different deuteration

The MSD for all four deuteration is shown in Fig. 7. The MSD values are lowest for D12 at all temperatures

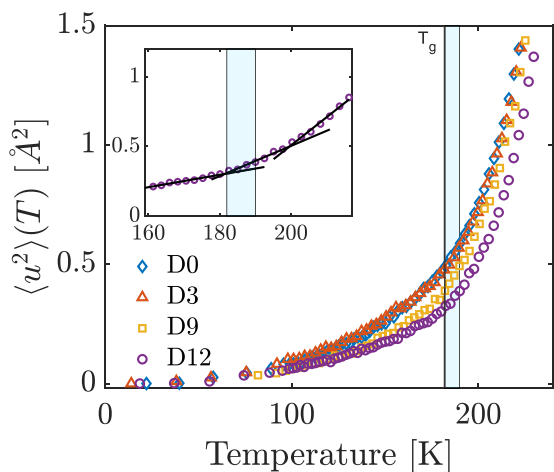


FIG. 7. Mean-square displacement (MSD) as a function of temperature for all four samples of Pyr14-TFSI. The blue shaded area illustrates the temperature region where the shear modulus measurements were performed. The inset is the data for D12 zoomed in around  $T_g$  in order to more clearly show three different regions with different dynamics revealed by two kinks in the MSD. This is illustrated by the solid black lines that are linear fits to the MSD in the specified region. The second kink is around 202 K, close to the temperature where the inelastic signal starts to increase significantly, see Fig. 3.

and increase with a decrease in deuteration. This is interpreted as additional motion from the methyl and butyl arms on the cation. The calculated MSD is connected to a motion faster than a nanosecond, and at low temperatures we assume that the MSD is completely vibrational. When relaxations enter the nanosecond regime, these also contribute to the calculated MSD. It is seen from the IFWS data in Fig. 3 that the relaxations enter at lower temperature for samples with nondeuterated alkyl groups. But the D12 is the only sample where the inelastic intensity is still low at the glass transition temperature  $T_g = 182 \text{ K}$ , meaning that the calculated MSD is connected to the vibrational MSD.

In the D12 sample where vibrations dominate the MSD there is a kink at  $T_g$  which can be understood in terms of the decrease in  $G_\infty$  at this temperature. The vibrational MSD is governed by the elastic moduli of the sample. In the simplest approximation it is proportional to temperature over the high-frequency shear modulus,  $\langle u^2 \rangle \propto T/G_\infty$  [26,59]. It is this temperature dependence of the elastic and vibrational properties above  $T_g$  that is related to the shoving model, and from this point of view it is the MSD data of the D12 sample that is most suitable for the purpose of testing the model.

While the D12 data are the cleanest in terms of excluding relaxational components from the vibrational MSD in the temperature range close to  $T_g$ , these data are hampered by the fact that the coherent contribution to the measured elastic intensity is rather high. The calculations of the MSD rely on the assumption that the data is purely incoherent, but as seen in Table I, this is far from true in D12. The coherent contribution can be seen directly in the  $Q$  dependence of the data in especially Fig. 6(b) where there is a clear shoulder at  $Q^2 \approx 1.9 \text{ \AA}^{-2}$  corresponding to  $Q = 1.4 \text{ \AA}^{-1}$ , which is the position of the main structure factor peak measured with the (coherent) x-ray scattering technique [6,28].

In conclusion, the D0 data give the cleanest signal in terms of being closest to the assumption of fully incoherent scattering, which is also visible in Fig. 6(a) where the coherent signal is close to zero, but there will be a contribution from relaxations. In contrast to this, the D12 data is the cleanest in terms of only containing vibrational MSD and no contribution

from relaxations, but there will be a higher coherent scattering contaminating the signal. D3 and D9 are intermediate situations. Thus data from all four samples are used in the MSD analysis.

## VII. TESTING THE SHOVING MODEL

From Fig. 5 it is seen that Pyr14-TFSI is a rather fragile liquid, similar to many van der Waals bonded liquids. This means that the  $\alpha$ -relaxation time depends more on temperature than a simple Arrhenius dependence. There is no consensus on what leads to this super-Arrhenius behavior, but one class of models suggests that it is due to the increase in the elastic moduli as the liquid approaches the glassy state. The shoving model assumes that the activation energy of the  $\alpha$  relaxation is proportional to the high-frequency shear modulus [60]. For liquids without a  $\beta$  relaxation, this high-frequency plateau can be measured with the PSG (see Refs. [18,26,61]); however, as we have shown, Pyr14-TFSI has a strong  $\beta$  relaxation and the high-frequency plateau lies beyond the frequency window of the technique. Another approach for testing the shoving model is to use the simplified harmonic approximation, which states that the vibrational MSD is proportional to temperature over high-frequency shear modulus,  $\langle u^2 \rangle \propto T/G_\infty$ . Both MSD data and high-frequency shear moduli have previously been used in tests of the shoving model [18], and it has been shown that the two methods were equivalent for van der Waals liquids with weak or no  $\beta$  relaxations [26]. The shoving model has been tested on a wide range of glass-forming liquids of different classes [18,26], but it has never before been tested on room-temperature ionic liquids.

The prediction of the shoving model is that the  $\alpha$ -relaxation time,  $\tau$ , is given by the following expression:

$$\log_{10} \tau(T) = (\log_{10} \tau_g - \log_{10} \tau_0) \frac{\langle u^2 \rangle_g}{\langle u^2 \rangle(T)} + \log_{10} \tau_0, \quad (4)$$

where  $\tau_0$  is the microscopic vibration time given by a phonon scale, and  $\tau_g$  is defined as the relaxation time at the glass transition.

The shoving model has been tested with MSD values from all four samples and  $\alpha$ -relaxation times from the shear mechanical spectra on the D0 sample. The reason we use four different data sets for finding the MSD values is that all of these methods rely on different assumptions and none of the methods are ideal; there is either coherent scattering or contributions from relaxation in the data. The different curves can in this sense be regarded as an estimate of the robustness of the shoving model test. The result is shown in Fig. 8, where the black solid line represents the shoving model prediction setting  $\log_{10} \tau_0 = -14$ . For all four MSD calculations the shoving model prediction works rather well. Figure 8 also shows the  $\alpha$ -relaxation time as an Angell plot, i.e., as a function of  $T_g/T$ . The black line corresponds to Arrhenius behavior when regarded with respect to the  $T_g/T$   $x$  axis. The closeness of the shoving model test compared to the Angell plot shows how much better the shoving model is compared to assuming an Arrhenius behavior. It is clear that the shoving model does a much better job in all the representations tested.

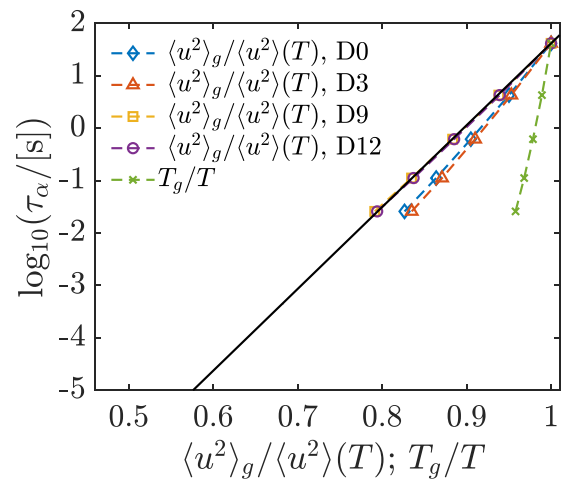


FIG. 8. A shoving plot with MSD data from for all four deuterations of Pyr14-TFSI with the shoving model prediction (black solid line). Relaxation time against  $\langle u^2 \rangle_g / \langle u^2 \rangle(T)$  and temperature for the standard Angell plot (crosses). The  $\alpha$  relaxation was found from the peak position of the shear mechanical  $\alpha$ -relaxation peak in Fig. 2(b), with  $\tau_\alpha = 1/(2\pi f_{\max})$ .

## VIII. CONCLUSION

In this work we have presented shear mechanical spectroscopy data, inverse ionic conductivity data found by dielectric spectroscopy, and quasielastic neutron fixed window scans on the room-temperature ionic liquid Pyr14-TFSI. From this we reveal features consistent with results on other RTILs, as well as additional features.

From the shear mechanical data we determine the temperature dependence of the  $\alpha$ -relaxation time in the supercooled region just above the glass transition temperature and find that Pyr14-TFSI has an Angell fragility of  $m_p = 85$ , which is consistent with previous results. The shear data also reveal a strong and temperature-independent  $\beta$  relaxation as well as a relaxation mode, seen as a wing in the spectrum, appearing between the  $\alpha$  relaxation and the  $\beta$  relaxation as the  $\alpha$  relaxation moves out of the frequency window of the PSG technique. Because our study is not limited to the somewhat small frequency ranges covered by conventional rheometers we are able to report these high-frequency modes in the ionic liquids.

Elastic and inelastic fixed window scans have been measured with the backscattering instrument IN16B on samples with different degrees of deuteration of the cation. It is demonstrated that the methyl group and the end methyl group on the butyl chain, both placed on the cation, give rise to dynamics which are faster than, and clearly separated from, the  $\alpha$  relaxation. By comparing the modes detected with the shear mechanical and neutron-backscattering techniques in a relaxation map it is found that the  $\alpha$  relaxation from both techniques have consistent behavior, as expected. It is, on the other hand, clear that the  $\beta$  relaxation and the wing seen in the shear spectra are unrelated to the methyl and butyl group dynamics observed with the neutron data. Consequently, a total of four distinct relaxational modes faster than the  $\alpha$  relaxation have been identified for Pyr14-TFSI. This rich dynamical picture is

maybe not surprising, given that an ionic liquid intrinsically is a binary system and that both van der Waals and Coulomb interactions play a role. Ionic liquids are also known to have structure on different length scales. The structure factor of Pyr14-TFSI reported in literature has a characteristic main structure factor peak as well as a peak at lower  $Q$  values which is believed to be associated with the charge ordering.

From the  $\alpha$ -relaxation and transport properties, we find that Pyr14-TFSI has a behavior similar to that of other simpler glass-forming liquids, since the temperature dependence of the shear mechanical  $\alpha$  relaxation is proportional to the resistivity (inverse ionic conductivity), showing that the viscous slowing down and the ionic conductivity are coupled, which is also shown in other studies on RTIL [30,54].

This picture of simple behavior in a structurally and dynamically complex ionic liquid is further strengthened by Pyr14-TFSI's compliance to the shoving model, which predicts that the temperature dependence of the  $\alpha$ -relaxation time is governed by the vibrational mean-square displacement, i.e.,

high-frequency rigidity. This is also the case in other, more simple classes of liquids [26]. Moreover, earlier work has shown that Pyr14-TFSI obeys density scaling of both  $\alpha$  relaxation and viscosity and resistivity [27–29].

The overall picture of this study is that while Pyr14-TFSI has complex structural features and rich dynamics, the  $\alpha$  relaxation has a behavior remarkably similar to that of other glass-forming liquids in that (1) ionic transport and structural relaxation is coupled as also proposed earlier, and (2) the temperature dependence of the  $\alpha$  relaxation is governed by high-frequency rigidity, through vibrational MSD, as predicted by the shoving model.

#### ACKNOWLEDGMENT

This work is part of the project RiDILiq, which is funded by the Independent Research Fund, Denmark.

- 
- [1] Z. Lei, B. Chen, Y.-M. Koo, and D. R. MacFarlane, Introduction: Ionic liquids, *Chem. Rev.* **117**, 6633 (2017).
- [2] A. Matic and B. Scrosati, Ionic liquids for energy applications, *MRS Bull.* **38**, 533 (2013).
- [3] E. Jónsson, Ionic liquids as electrolytes for energy storage applications—A modelling perspective, *Energy Storage Mater.* **25**, 827 (2020).
- [4] A. Triolo, O. Russina, H.-J. Bleif, and E. Di Cola, Nanoscale segregation in room temperature ionic liquids, *J. Phys. Chem. B* **111**, 4641 (2007).
- [5] A. Triolo, O. Russina, B. Fazio, G. B. Appetecchi, M. Carewska, and S. Passerini, Nanoscale organization in piperidinium-based room temperature ionic liquids, *J. Chem. Phys.* **130**, 164521 (2009).
- [6] L. Aguilera, J. Vlkner, A. Labrador, and A. Matic, The effect of lithium salt doping on the nanostructure of ionic liquids, *Phys. Chem. Chem. Phys.* **17**, 27082 (2015).
- [7] A. M. Fleshman and N. A. Mauro, Temperature-dependent structure and transport of ionic liquids with short-and intermediate-chain length pyrrolidinium cations, *J. Mol. Liq.* **279**, 23 (2019).
- [8] S. Li, J. L. Bañuelos, J. Guo, L. Anovitz, G. Rother, R. W. Shaw, P. C. Hillesheim, S. Dai, G. A. Baker, and P. T. Cummings, Alkyl chain length and temperature effects on structural properties of pyrrolidinium-based ionic liquids: A combined atomistic simulation and small-angle x-ray scattering study, *J. Phys. Chem. Lett.* **3**, 125 (2012).
- [9] T. Mackoy, N. A. Mauro, and R. A. Wheeler, Temperature dependence of static structure factor peak intensities for a pyrrolidinium-based ionic liquid, *J. Phys. Chem. B* **123**, 1672 (2019).
- [10] C. S. Santos, N. S. Murthy, G. A. Baker, and E. W. Castner, Communication: X-ray scattering from ionic liquids with pyrrolidinium cations, *J. Chem. Phys.* **134**, 121101 (2011).
- [11] C. A. Angell, Relaxation in liquids, polymers and plastic crystals—Strong fragile patterns and problems, *J. Non-Cryst. Solids* **131-133**, 13 (1991).
- [12] P. Sippel, P. Lunkenheimer, S. Krohns, E. Thoms, and A. Loidl, Importance of liquid fragility for energy applications of ionic liquids, *Sci. Rep.* **5**, 13922 (2015).
- [13] C. Gainaru, R. Figuli, T. Hecksher, B. Jakobsen, J. C. Dyre, M. Wilhelm, and R. Böhmer, Shear-Modulus Investigations of Monohydroxy Alcohols: Evidence for a Short-Chain-Polymer Rheological Response, *Phys. Rev. Lett.* **112**, 098301 (2014).
- [14] K. Adrjanowicz, B. Jakobsen, T. Hecksher, K. Kaminski, M. Dulski, M. Paluch, and K. Niss, Communication: Slow supramolecular mode in amine and thiol derivatives of 2-ethyl-1-hexanol revealed by combined dielectric and shear-mechanical studies, *J. Chem. Phys.* **143**, 181102 (2015).
- [15] M. H. Jensen, C. Gainaru, C. Alba-Simionesco, T. Hecksher, and K. Niss, Slow rheological mode in glycerol and glycerol-water mixtures, *Phys. Chem. Chem. Phys.* **20**, 1716 (2018).
- [16] S. Arrese-Igor, A. Alegría, and J. Colmenero, Multimodal character of shear viscosity response in hydrogen bonded liquids, *Phys. Chem. Chem. Phys.* **20**, 27758 (2018).
- [17] T. Cosby, Z. Vicars, Y. Wang, and J. Sangoro, Dynamic-mechanical and dielectric evidence of long-lived mesoscale organization in ionic liquids, *J. Phys. Chem. Lett.* **8**, 3544 (2017).
- [18] T. Hecksher and J. C. Dyre, A review of experiments testing the shoving model, *J. Non-Cryst. Solids* **407**, 14 (2015).
- [19] F. S. Howell, R. A. Bose, P. B. Macedo, and C. T. Moynihan, Electrical relaxation in a glass-forming molten salt, *J. Phys. Chem.* **78**, 639 (1974).
- [20] A. Rivera, A. Brodin, A. Pugachev, and E. A. Rössler, Orientational and translational dynamics in room temperature ionic liquids, *J. Chem. Phys.* **126**, 114503 (2007).
- [21] J. R. Sangoro, A. Serghei, S. Naumov, P. Galvosas, J. Kärger, C. Wespe, F. Bordusa, and F. Kremer, Charge transport and mass transport in imidazolium-based ionic liquids, *Phys. Rev. E* **77**, 051202 (2008).
- [22] Z. Wojnarowska and M. Paluch, Recent progress on dielectric properties of protic ionic liquids, *J. Phys.: Condens. Matter* **27**, 073202 (2015).

- [23] W. Tu, G. Szklarz, K. Adrjanowicz, K. Grzybowska, J. Knapik-Kowalczyk, and M. Paluch, Effect of cation *n*-alkyl side-chain length, temperature, and pressure on the glass-transition dynamics and crystallization tendency of the [c n c l pyr] + [tf2n]- ionic liquid family, *J. Phys. Chem. C* **123**, 12623 (2019).
- [24] J. C. Dyre, Colloquium: The glass transition and elastic models of glass-forming liquids, *Rev. Mod. Phys.* **78**, 953 (2006).
- [25] J. C. Dyre, T. Christensen, and N. B. Olsen, Elastic models for the non-Arrhenius viscosity of glass-forming liquids, *J. Non-Cryst. Solids* **352**, 4635 (2006).
- [26] H. W. Hansen, B. Frick, T. Hecksher, J. C. Dyre, and K. Niss, Connection between fragility, mean-squared displacement and shear modulus in two van der Waals bonded glass-forming liquids, *Phys. Rev. B* **95**, 104202 (2017).
- [27] K. R. Harris and M. Kanakubo, Self-diffusion, velocity cross-correlation, distinct diffusion and resistance coefficients of the ionic liquid [BMIM][Tf<sub>2</sub>N] at high pressure, *Phys. Chem. Chem. Phys.* **17**, 23977 (2015).
- [28] H. W. Hansen, F. Lundin, K. Adrjanowicz, B. Frick, A. Matic, and K. Niss, Density scaling of structure and dynamics of an ionic liquid, *Phys. Chem. Chem. Phys.* **22**, 14169 (2020).
- [29] F. Lundin, H. W. Hansen, K. Adrjanowicz, B. Frick, D. Rauber, R. Hempelmann, O. Shebanova, K. Niss, and A. Matic, Pressure and temperature dependence of local structure and dynamics in an ionic liquid, *J. Phys. Chem. B* **125**, 2719 (2021).
- [30] A. Martinelli, A. Matic, P. Jacobsson, L. Börjesson, A. Fernicola, and B. Scrosati, Phase behavior and ionic conductivity in lithium bis(trifluoromethanesulfonyl)imide-doped ionic liquids of the pyrrolidinium cation and bis(trifluoromethanesulfonyl)imide anion, *J. Phys. Chem. B* **113**, 11247 (2009).
- [31] M. Kunze, S. Jeong, E. Paillard, M. Schonhoff, M. Winter, and S. Passerini, New insights to self-aggregation in ionic liquid electrolytes for high-energy electrochemical devices, *Adv. Energy Mater.* **1**, 274 (2011).
- [32] K. R. Harris, L. A. Woolf, M. Kanakubo, and T. Rütger, Transport properties of *N*-butyl-*N*-methylpyrrolidinium bis(trifluoromethylsulfonyl)amide, *J. Chem. Eng. Data* **56**, 4672 (2011).
- [33] F. M. Vitucci, D. Manzo, M. A. Navarra, O. Palumbo, F. Trequattrini, S. Panero, P. Bruni, F. Croce, and A. Paolone, Low-temperature phase transitions of 1-butyl-1-methylpyrrolidinium bis(trifluoromethanesulfonyl)imide swelling a polyvinylidene fluoride electrospun membrane, *J. Phys. Chem. C* **118**, 5749 (2014).
- [34] E. Zorebski, M. Zorebski, M. Dzida, P. Goodrich, and J. Jacquemin, Isobaric and isochoric heat capacities of imidazolium-based and pyrrolidinium-based ionic liquids as a function of temperature: Modeling of isobaric heat capacity, *Ind. Eng. Chem. Res.* **56**, 2592 (2017).
- [35] R. Ge, C. Hardacre, J. Jacquemin, P. Nancarrow, and D. W. Rooney, Heat capacities of ionic liquids as a function of temperature at 0.1 mPa. measurement and prediction, *J. Chem. Eng. Data* **53**, 2148 (2008).
- [36] E. W. Castner, J. F. Wishart, and H. Shirota, Intermolecular dynamics, interactions, and solvation in ionic liquids, *Acc. Chem. Res.* **40**, 1217 (2007).
- [37] H. Shirota, A. M. Funston, J. F. Wishart, and E. W. Castner, Jr., Ultrafast dynamics of pyrrolidinium cation ionic liquids, *J. Chem. Phys.* **122**, 184512 (2005).
- [38] See Supplemental Material at <http://link.aps.org/supplemental/10.1103/PhysRevMaterials.5.065606> for detailed description of the data analysis used in this study [[62,63]].
- [39] C. D. Tran, S. H. De Paoli Lacerda, and D. Oliveira, Absorption of water by room-temperature ionic liquids: Effect of anions on concentration and state of water, *Appl. Spectrosc.* **57**, 152 (2003).
- [40] T. Christensen and N. B. Olsen, A rheometer for the measurement of a high shear modulus covering more than seven decades of frequency below 50 kHz, *Rev. Sci. Instrum.* **66**, 5019 (1995).
- [41] B. Igarashi, T. Christensen, E. H. Larsen, N. B. Olsen, I. H. Pedersen, T. Rasmussen, and J. C. Dyre, An impedance-measurement setup optimized for measuring relaxations of glass-forming liquids, *Rev. Sci. Instrum.* **79**, 045106 (2008).
- [42] B. Igarashi, T. Christensen, E. H. Larsen, N. B. Olsen, I. H. Pedersen, T. Rasmussen, and J. C. Dyre, A cryostat and temperature control system optimized for measuring relaxations of glass-forming liquids, *Rev. Sci. Instrum.* **79**, 045105 (2008).
- [43] B. Frick, J. Combet, and L. van Eijck, New possibilities with inelastic fixed window scans and linear motor Doppler drives on high resolution neutron backscattering spectrometers, *Nucl. Instrum. Methods Phys. Res., Sect. A* **669**, 7 (2012).
- [44] M. Busch, T. Hofmann, B. Frick, J. P. Embs, B. Dyatkin, and P. Huber, Ionic liquid dynamics in nanoporous carbon: A pore-size- and temperature-dependent neutron spectroscopy study on supercapacitor materials (2020).
- [45] D. Richard, M. Ferrand, and G. J. Kearley, Analysis and visualisation of neutron-scattering data, *J. Neutron Res.* **4**, 33 (1996).
- [46] T. Cosby, Z. Vicars, M. Heres, K. Tsunashima, and J. Sangoro, Dynamic and structural evidence of mesoscopic aggregation in phosphonium ionic liquids, *J. Chem. Phys.* **148**, 193815 (2018).
- [47] O. Palumbo, F. Trequattrini, F. M. Vitucci, and A. Paolone, Relaxation dynamics and phase transitions in ionic liquids: Viscoelastic properties from the liquid to the solid state, *J. Phys. Chem. B* **119**, 12905 (2015).
- [48] T. Hecksher, N. B. Olsen, and J. C. Dyre, Model for the alpha and beta shear-mechanical properties of supercooled liquids and its comparison to squalane data, *J. Chem. Phys.* **146**, 154504 (2017).
- [49] B. Jakobsen, K. Niss, C. Maggi, N. B. Olsen, T. Christensen, and J. C. Dyre, Beta relaxation in the shear mechanics of viscous liquids: Phenomenology and network modeling of the alpha-beta merging region, *J. Non-Cryst. Solids* **357**, 267 (2011).
- [50] T. Burankova, G. Simeoni, R. Hempelmann, J. F. Mora Cardozo, and J. P. Embs, Dynamic heterogeneity and flexibility of the alkyl chain in pyridinium-based ionic liquids, *J. Phys. Chem. B* **121**, 240 (2017).
- [51] T. Burankova, E. Reichert, V. Fossog, R. Hempelmann, and J. P. Embs, The dynamics of cations in pyridinium-based ionic liquids by means of quasielastic- and inelastic neutron scattering, *J. Mol. Liq.* **192**, 199 (2014).
- [52] R. Böhmer and C. A. Angell, Correlations of the nonexponentiality and state dependence of mechanical relaxations with bond connectivity in Ge-As-Se supercooled liquids, *Phys. Rev. B* **45**, 10091 (1992).
- [53] R. Böhmer, K. L. Ngai, C. A. Angell, and D. J. Plazek, Non-exponential relaxations in strong and fragile glass formers, *J. Chem. Phys.* **99**, 4201 (1993).

- [54] C. J. Jafta, C. Bridges, L. Haupt, C. Do, P. Sippel, M. J. Cochran, S. Krohns, M. Ohl, A. Loidl, E. Mamontov, P. Lunkenheimer, S. Dai, and X.-G. Sun, Ion dynamics in ionic-liquid-based li-ion electrolytes investigated by neutron scattering and dielectric spectroscopy, *ChemSusChem* **11**, 3512 (2018).
- [55] G. P. Johari, Glass transition and secondary relaxations in molecular liquids and crystals, *Ann. N.Y. Acad. Sci.* **279**, 117 (1976).
- [56] A. Rahman, K. S. Singwi, and A. Sjölander, Theory of slow neutron scattering by liquids. I, *Phys. Rev.* **126**, 986 (1962).
- [57] R. Zorn, Multiple scattering correction of neutron scattering elastic scans, *Nucl. Instrum. Methods Phys. Res., Sect. A* **572**, 874 (2007).
- [58] R. Zorn, On the evaluation of neutron scattering elastic scan data, *Nucl. Instrum. Methods Phys. Res., Sect. A* **603**, 439 (2009).
- [59] J. C. Dyre and N. B. Olsen, Landscape equivalent of the shoving model, *Phys. Rev. E* **69**, 042501 (2004).
- [60] J. C. Dyre, N. B. Olsen, and T. Christensen, Local elastic expansion model for viscous-flow activation energies of glass-forming molecular liquids, *Phys. Rev. B* **53**, 2171 (1996).
- [61] B. Jakobsen, K. Niss, and N. B. Olsen, Dielectric and shear mechanical alpha and beta relaxations in seven glass-forming liquids, *J. Chem. Phys.* **123**, 234511 (2005).
- [62] F. Kremer and A. Schönhalz (editors), *Broadband Dielectric Spectroscopy* (Springer, Berlin, 2003).
- [63] P. Thompson, D. E. Cox, and J. B. Hastings, Rietveld refinement of Debye-Scherrer synchrotron x-ray data from  $\text{Al}_2\text{O}_3$ , *J. Appl. Crystallogr.* **20**, 79 (1987).